LANGMUIR

pubs.acs.org/Langmuir Article

Curvature-Mediated Forces on Elastic Inclusions in Fluid Interfaces

Joseph M. Barakat and Todd M. Squires*

Cite This: *Langmuir* 2022, 38, 1099–1105 Read Online

ACCESS | Metrics & More | Article Recommendations | Supporting Information

ABSTRACT: Heterogeneous fluid interfaces often include two-dimensional solid domains that mechanically respond to changes in interfacial curvature. While this response is well-characterized for rigid inclusions, the influence of solid-like elasticity remains essentially unexplored. Here, we show that an initially flat, elastic inclusion embedded in a curved, fluid interface will exhibit qualitatively distinct behavior depending on its size and stiffness. Small, stiff inclusions are limited by bending and experience forces directed up gradients of Gaussian curvature, in keeping with prior findings for rigid discoids. By contrast, larger and softer inclusions are driven down gradients of squared Gaussian curvature in order to minimize the elastic penalty for stretching. Our calculations of the force on a solid inclusion are shown to collapse onto a universal curve spanning the bending- and stretching-limited regimes. From these results, we make predictions for the curvature-directed motion of deformable solids embedded within a model interface of variable Gaussian curvature.

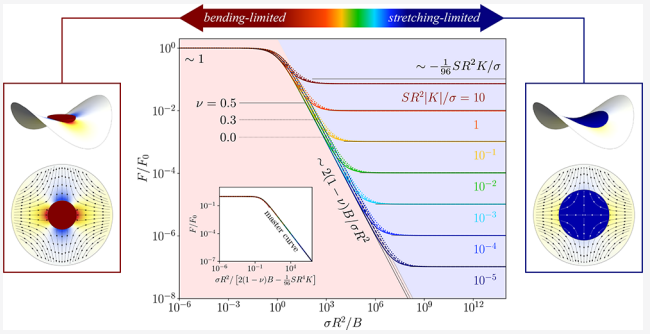

INTRODUCTION

Two-dimensional (2D) solid domains naturally emerge at fluid interfaces in biological systems and multiphase materials. Examples include solid−fluid coexisting phases in lipid monolayers[1−5] and bilayers,[6−10] lipid rafts,[11−14] membrane-bound protein clusters,[15−18] and interfacial colloidal crystals.[19−21] Solid inclusions differ from 2D fluids in their response to changes in interfacial curvature. Whereas fluid molecules can freely rearrange within an interface to adapt to its curvature, molecules in a 2D solid remember the positions of their neighbors and can only change their Gaussian curvature by stretching.[22] Elastic strains due to Gaussian curvature can cause confined thin sheets to buckle[23] and alter the growth pathway of solid crystals in vesicles[16,24] and colloidosomes.[20,21]

The present work addresses the behavior of solid inclusions in interfaces with an *inhomogeneous* Gaussian curvature, as observed in the tubular membranes of cellular organelles,[25,26] the branching network of the lung alveoli,[27] and the tortuous, intercalating phases of particle-stabilized bijels.[28,29] Prior work in the colloidal physics literature[30−35] has shown that rigid particles trapped at an interface tend to migrate down gradients of Gaussian curvature, due to contact-line irregularities that distort the surrounding interface. We recently showed[36] that planar particles—those with pinned, but nonundulated contact lines—migrate *up* such gradients, toward regions of high Gaussian curvature. However, it is not at all clear which behavior is expected for *deformable* solid inclusions that are bent or stretched by the embedding interface. This can occur if the inclusions are appreciably soft—e.g., self-assembled domains held together by weak bonds[37]—or thin—e.g., covalently bonded, single-layer materials, such as graphene.[38] These examples raise two basic questions: (i) Under what conditions will solid inclusions deform under the action of interfacial tension? (ii) How does their deformability impact the forces exerted on them by interfacial curvature?

To answer these questions, we analyze the force, $\boldsymbol{F}$, exerted on a single, circular inclusion embedded within a gradient of Gaussian curvature, K. The inclusion is modeled as an elastic plate, following the well-established theory of Föppl and von Kármán.[22] Our analysis reveals the significant consequences of solid-like elasticity on curvature-mediated forces. For inclusions that are not easily bent, these forces are directed along the curvature gradient, $\boldsymbol{F} \propto \nabla K$, in agreement with our previous findings[36] for rigid, planar particles. However, inclusions that are easy to bend but comparably difficult to stretch exhibit a qualitatively different behavior, $\boldsymbol{F} \propto -\nabla K^2$, with the force directed *against* the gradient of the *squared* Gaussian curvature. We show that the transition between these two regimes can be achieved by increasing the lateral dimension of the inclusion. Thus, we identify an important distinction: whereas small, stiff inclusions are driven toward

Received: October 11, 2021
Revised: December 28, 2021
Published: January 11, 2022

https://doi.org/10.1021/acs.langmuir.1c02709
Langmuir 2022, 38, 1099−1105

interfacial regions of high Gaussian curvature, larger and softer inclusions are attracted to regions of *zero* Gaussian curvature (Figure 1). This result is reminiscent of the energetic penalty

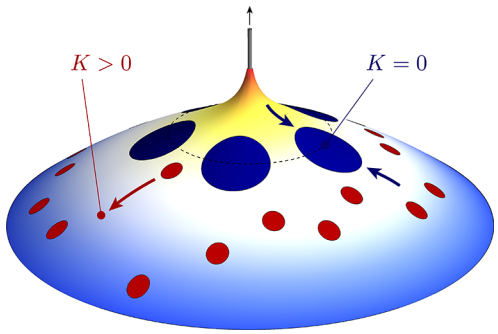

Figure 1. Schematic of 2D solid inclusions embedded within a curved, fluid interface. The interface is shaped into a "teardrop" by applying an internal pressure and a local, transverse force. Curvature-mediated forces drive small, stiff inclusions (red, bending-limited) away from the "tip" toward the "globe", where the Gaussian curvature is positive. By contrast, large, soft inclusions (blue, stretching-limited) are driven toward the inflection line where the Gaussian curvature vanishes.

for wrapping a thin, elastic disk around a sphere ($K \neq 0$) as compared to a cylinder ($K = 0$). Our findings have potential implications for not only biological systems but also a wide range of *elastocapillary* phenomena, such as kirigami and origami,[39] bundling of wet fibers,[40] and capillary wrinkling.[41]

METHODOLOGY

In the following theoretical development, we consider a curved fluid interface under tension, σ, with a static pressure drop, p, applied across the interface. A local patch of the interface is described by its displacement, $w_f(\boldsymbol{r})$, above or below a point $\boldsymbol{r}$ in the 2D plane. For small displacements, the Young−Laplace law states that

$$\sigma\nabla^2 w_f = -p \tag{1}$$

in the *fluid region* outside any interface-embedded, solid inclusions. Within any given *solid region*, elastic stresses must be taken into account. According to the weakly nonlinear theory of elastic plates,[22,42] the solid displacement, $w_s(\boldsymbol{r})$, and Airy stress function, $\chi(\boldsymbol{r})$, are governed by the Föppl−von Kármán equations:

$$B\nabla^4 w_s - \mathcal{L}^4(\chi, w_s) = p \tag{2a}$$

$$S^{-1}\nabla^4\chi + \frac{1}{2}\mathcal{L}^4(w_s, w_s) = 0 \tag{2b}$$

where S is the stretching modulus, B is the bending modulus, and $\mathcal{L}^4(\phi,\psi) \equiv (\nabla^2\phi)(\nabla^2\psi) - (\nabla\nabla\phi):(\nabla\nabla\psi)$. In classical plate theory

$$S = Eh \tag{3a}$$

$$B = \frac{Eh^3}{12(1-\nu^2)} \tag{3b}$$

where E is Young's modulus, ν is the Poisson ratio, and h is the plate thickness. Thus, the characteristic thickness of a solid inclusion scales as $h \sim \sqrt{B/S}$. The boundary conditions associated with eqs 1 and 2 enforce continuity of w, forces, and torques across the border Γ of any given inclusion (for the detailed equations, see the Supporting Information).

If the inclusions were absent, then the interface would adopt its native shape, $w_0(\boldsymbol{r})$, satisfying eq 1. Under a static pressure, the mean curvature of the interface, H, is spatially uniform, whereas the Gaussian curvature, $K(\boldsymbol{r})$, can vary with position:

$$2H = \nabla^2 w_0 = -p/\sigma \tag{4a}$$

$$2K = \mathcal{L}^4(w_0, w_0) \tag{4b}$$

The sign of K dictates the "character" of the interface: regions with $K > 0$ have two nonzero principal curvatures of like sign (e.g., spheres and paraboloids); $K < 0$ implies oppositely signed curvatures (e.g., catenoids and saddles); finally, $K = 0$ indicates the vanishing of at least one principal curvature (e.g., cylinders and planes). For interfaces with constant mean curvature (as required by eq 1), the Gaussian curvature is maximized when the two principal curvatures are equal, $K_{max} \equiv H^2$.

Embedding a solid inclusion into the interface produces a quadrupolar disturbance, $\delta w_f(\boldsymbol{r}) \sim 1/r^2$, giving a total displacement, $w_f = w_0 + \delta w_f$, in the fluid region. The disturbance couples to the background curvature to produce a net force on the inclusion, given by[36,43]

$$\boldsymbol{F} = -\sigma\oint_\Gamma \Sigma^2(w_0, \delta w_f)\cdot d\boldsymbol{s} \tag{5}$$

where Γ is the boundary enclosing the inclusion (evaluated in the fluid region), $\Sigma^2(\phi,\psi) \equiv \nabla\phi\nabla\psi + \nabla\psi\nabla\phi - (\nabla\phi\cdot\nabla\psi)\mathbf{I}$, and $\mathbf{I}$ is the 2D unit tensor. We have numerically solved eqs 1 and 2 for the disturbance due to a circular inclusion embedded in a gradient of Gaussian curvature using the finite difference method (details are given in the Supporting Information) and used eq 5 to calculate the resulting force on the inclusion. Two limiting cases, which are particularly illustrative, arise when either the bending stiffness, B, or the stretching stiffness, S, limits the deformation of the inclusion. These are discussed separately, below.

RESULTS AND DISCUSSION

Bending-Limited Regime. Stiff inclusions in weakly curved interfaces admit deflections much smaller than their characteristic thickness ($w_s \ll h$). In this limit, the nonlinear stretching term in eq 2b is relatively small and may be neglected. Integrating eq 2b with the boundary conditions $\partial\chi/\partial r = 2\chi/r = \sigma r$ on Γ gives $\chi = \frac{1}{2}\sigma r^2$ in the solid region. Equation 2a then simplifies to the classical plate equation:

$$B\nabla^4 w_s - \sigma\nabla^2 w_s = p = -2\sigma H \tag{6}$$

which is linear in the displacement field.

Equations 1 and 6 may be solved analytically for a circular inclusion of radius R via modified Bessel functions (details of this analysis are given in the Supporting Information). The resulting displacement disturbance, $\delta w = w - w_0$, and displacement gradient, ∇w, are sketched in Figure 2 for inclusion radii smaller or larger than the characteristic "bending radius":

$$R_B = \sqrt{\frac{2(1-\nu)B}{\sigma}} \tag{7}$$

https://doi.org/10.1021/acs.langmuir.1c02709
Langmuir 2022, 38, 1099−1105

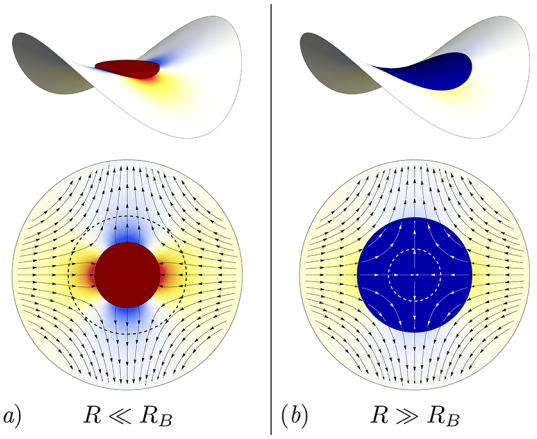

Figure 2. 3D and 2D projections of the displacement disturbance, δw (density plots), and displacement gradient, ∇w (stream plots), surrounding (a) a small, stiff inclusion ($R \ll R_B$) and (b) a large, soft inclusion ($R \gg R_B$) embedded in an interface with locally anisotropic curvature. The bending radius R_B is indicated by the dashed circle.

This length scale is closely related to the "bendocapillary length" defined by Style et al.[44] A thin disk of a stiff plastic pinned to an oil–water interface (h = 1 μm, E = 1 GPa, ν = 0.5, σ = 50 mN/m) has $R_B \approx 50$ μm according to eqs 3b and 7. Inclusions smaller than this radius ($R \ll R_B$) are effectively rigid and resist changing their curvature. Such inclusions bend the displacement gradient lines into an orientation normal to their boundaries, producing the maximum deflection of the interface (Figure 2a). By contrast, inclusions large enough to be bent by the interface ($R \gg R_B$) conform to the host interface shape and admit a much weaker, almost imperceivable disturbance (Figure 2b).

Substituting the displacement disturbance, $\delta w_f = w_f - w_0$, into eq 5 gives the force on the inclusion, $\boldsymbol{F}$. A closed-form, though somewhat unwieldy, expression for $\boldsymbol{F}$ is derived in the Supporting Information (eqs S.9 and S.13). Here, we only analyze its two limits for small and large R. For small, stiff inclusions, we recover our previous result for rigid, planar particles,[36] which we denote by $\boldsymbol{F}_0$:

$$\boldsymbol{F} = \frac{1}{2}\pi\sigma R^4 \nabla K \equiv \boldsymbol{F}_0, \quad R \ll R_B \tag{8a}$$

However, large, soft inclusions that can bend out of plane experience much weaker forces that are attenuated by a factor of R_B^2/R^2 (cf. eq 7):

$$\boldsymbol{F} = \pi(1-\nu)BR^2\nabla K = \frac{1}{2}\pi\sigma R_B^2 R^2 \nabla K, \quad R \gg R_B \tag{8b}$$

Notably, both limits 8 predict that the inclusion is driven *up* the curvature gradient, $\boldsymbol{F} \propto \nabla K$. The maximum possible value of K is $K_{max} = H^2$, at which point the interface is *isotropic* (e.g., spheres and planes). In the Supporting Information (cf. eq S.13), it is shown that the force is proportional to the negative gradient of $H^2 - K$, that is, the squared *deviatoric* curvature. For tense interfaces under a static pressure, eq 1 stipulates that the mean curvature is uniform and, therefore, only the Gaussian curvature varies with position; hence, $\nabla H = 0$ and $-\nabla(H^2 - K) = \nabla K$, recovering eqs 8.

Stretching-Limited Regime. In addition to bending, inclusions may bend significantly enough that stretching can no longer be ignored. For sufficiently large displacements ($w_s \gg h$), the nonlinear stretching stresses in eqs 2 dominate over the bending stresses. Analytical progress is possible if the displacement and stress function *within* the solid inclusion are weakly perturbed from an interface-conforming base state, $w_s = w_0 + \delta w_s$ and $\chi = \frac{1}{2}\sigma r^2 + \delta\chi$. Under these restrictions, the Föppl-von Kármán eqs 2 simplify to a set of linear equations for the perturbation fields, δw_s and $\delta\chi$:

$$\sigma\nabla^2\delta w_s = -\mathcal{L}^4(w_0, \delta\chi) \tag{9a}$$

$$S^{-1}\nabla^4\delta\chi = -\frac{1}{2}\mathcal{L}^4(w_0, w_0) = -K \tag{9b}$$

where the last term reveals that Gaussian curvature forces the small departure from uniform and isotropic stretching. Equations 9 are valid under two conditions: (i) bending stresses are negligible compared to stretching stresses, and (ii) stretching stresses contribute a small correction to the isotropic tension exerted by the interface. Mathematically, these can be summarized by the joint inequalities, $\sigma \gg SR^2|K| \gg B/R^2$.

We have solved eqs 1 and 9 analytically for a circular inclusion in a macroscopic gradient (details of this solution are given in the Supporting Information). Applying eq 5 and setting $\nabla H = 0$ gives the force

$$\boldsymbol{F} = -\frac{1}{192}\pi SR^6 K\nabla K = -\frac{1}{384}\pi SR^6\nabla K^2 \tag{10}$$

where the additional factor of K, relative to eqs 8, arises from the anisotropic strain incurred by stretching. Thus, stretching-limited inclusions are driven *down* gradients of the *squared* Gaussian curvature, $\boldsymbol{F} \propto -\nabla K^2$. Since K^2 is minimized when $K = 0$, this implies a driving force toward *developable surfaces* (e.g., cylinders and planes). Physically, this driving force reflects the energetic cost of changing the inclusion's intrinsic Gaussian curvature.

Equation 10 bears obvious resemblance to the force computed by Aharoni et al.[45] using a virtual work argument (see eq 8 in their article and the short discussion thereafter). In their work, the authors considered an elastic, 2D disk with intrinsic Gaussian curvature, K_{disk}, embedded in a 2D surface with dissimilar Gaussian curvature, K, assuming the bending elasticity of the disk to be negligible. The geometric incompatibility between the disk and the embedding surface gives rise to residual elastic energy and a net force down gradients in $(K - K_{disk})^2$. Our result for the stretching-dominated limit (eq 10), which was derived by direct integration of stresses along the boundary of the inclusion (cf. eq 5), exactly agrees with the virtual work calculation of Aharoni et al.[45] for the special case of planar disks, $K_{disk} = 0$.

In addition, eq 10 was derived by assuming that elastic stresses to due to stretching are small in comparison to the interfacial tension, $\sigma \gg SR^2|K|$. Numerical solutions of eqs 1 and 2 are not subject to this restriction; calculations were performed for values of $SR^2|K|/\sigma$ as large as 10. For these larger values, the scaling $\boldsymbol{F} \propto -\nabla K^2$ still holds, albeit with a numerical prefactor that differs from eq 10. Converged numerical solutions were not obtained for values of $SR^2|K|/\sigma$ much larger than 10. It is expected, based on literature precedent,[41,46] that an elastic inclusion would exhibit a wrinkling instability above a critical threshold of $SR^2|K|/\sigma$ (e.g., for small enough tensions). In such wrinkled states, resistance to bending can no longer be ignored. This regime, where $SR^2|K|/\sigma \gg 1$, is beyond the scope of the present work.

https://doi.org/10.1021/acs.langmuir.1c02709
Langmuir 2022, 38, 1099−1105

From the intersection of eqs 8b and 10, we identify a second crossover radius:

$$R_S = \left(\frac{192(1-\nu)B}{S|K|}\right)^{1/4} \tag{11}$$

which depends upon the local Gaussian curvature, $K(r)$. For an isotropic, continuum-elastic plate, it can be readily deduced (from eqs 3, 4, and 11) that the crossover $R = R_S$ roughly corresponds to displacements on the order of the plate thickness, $w_s \sim h$. Inclusions of size $R \gg R_S$ resist stretching and admit forces given by eq 10. Since eq 10 is a perturbative approximation of the stretching-limited force, R_S is only physically meaningful if $R_S \gg R_B$ or, equivalently, if $\sigma^2 \gg \frac{1}{48}(1-\nu)BS|K|$. Practically, it is useful to think of this as a restriction on the elastic stiffness of the solid phase for the scale separation to hold. For example, taking $\sigma = 50$ mN/m, $h = 1$ μm, and $|K|^{-1/2} = 100$ μm as fixed parameters (corresponding to a thin disk suspended at the oil−water interface of a microdroplet), the scale separation, $R_S/R_B \gg 1$, breaks down above a critical Young's modulus, $E \approx 120$ MPa.

Comparison between Analytical and Numerical Results. Figure 3 compares analytical predictions for the force, eqs 8 and 10, to numerical calculations (using the finite difference method) for a range of values of $\sigma R^2/B$, $SR^2|K|/\sigma$, and ν under zero pressure, $p = 0$. In the plots, the magnitude of the force, $|\boldsymbol{F}| \equiv F$, is scaled by F_0, the force on a rigid, planar particle (cf. eq 8a). Excellent agreement between the numerics and analytics is achieved over a wide range of parameters. Several regimes are identified:

- For $R \ll R_B$, the inclusion is effectively rigid and $F/F_0 \sim 1$ (eq 8a).
- In the intermediate regime, where $R_B \ll R \ll R_S$, the inclusion is soft enough to bend out of plane but not so soft to incur significant stretching; this gives a weaker force $F/F_0 \sim 2(1-\nu)B/\sigma R^2$ (eq 8b).
- Finally, for $R_B \ll R_S \ll R$, the deformation of the inclusion is large and limited by resistance to stretching; eq 10 predicts $F/F_0 \sim -\frac{1}{96}SR^2K/\sigma$ in this regime.

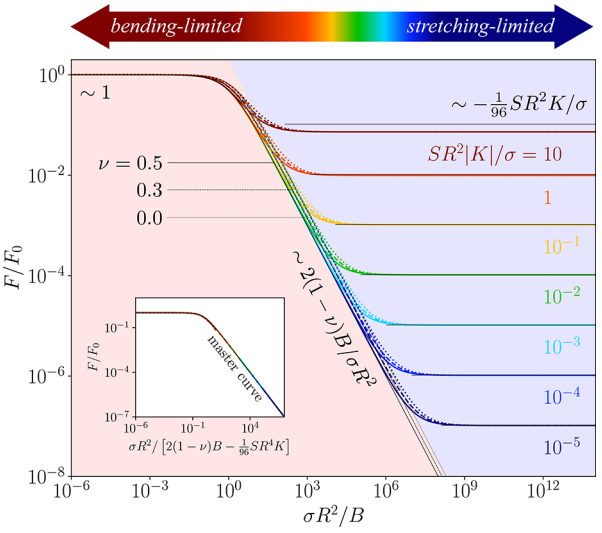

Figure 3. Dimensionless force on a circular inclusion, F/F_0, plotted against $\sigma R^2/B$ for different values of $SR^2|K|/\sigma$ and ν with $p = 0$ and $K < 0$. Colored curves represent numerical computations; lightened, black curves show the asymptotic predictions of eqs 8 and 10. Inset: Redefining the abscissae collapses all numerical data onto a "master curve" (eq 12).

- Finally, for $R_B \ll R_S \ll R$, the deformation of the inclusion is large and limited by resistance to stretching; eq 10 predicts $F/F_0 \sim -\frac{1}{96}SR^2K/\sigma$ in this regime.

Significant deviations from eq 10 are observed only at the largest reported value of $SR^2|K|/\sigma = 10$, which is well outside the range of validity of the perturbative approximation. Within the scope of this approximation, a "master curve"

$$\boldsymbol{F} \approx \frac{\boldsymbol{F}_0}{1 + \frac{\sigma R^2}{2(1-\nu)B - \frac{1}{96}SR^4K}} \tag{12}$$

successfully collapses all of the numerical results (Figure 3, inset). It can be readily verified that eq 12 degenerates to eqs 8 and 10 in the appropriate limits.

Numerical results for finite pressures ($p \neq 0$) are presented in the Supporting Information (Figure S.1). Introducing a finite pressure jump across the interface uniformly shifts the Gaussian curvature without altering its gradient. Consequently, pressure affects only those forces that are limited by resistance to stretching, through the factor of K appearing in eq 10. The bending-limited force, eq 8, depends only upon the gradient of K and is unaffected by a change in the pressure.

Model Interface. We now turn our attention to a model interface formed by a static pressure p and a force q applied to a small ring of radius a centered at the origin:

$$w_0 = -\frac{p}{4\sigma}r^2 - \frac{q}{2\pi\sigma}\log\left(\frac{r}{a}\right) \tag{13}$$

where it is assumed that $\pi a^2 p \ll q$. The surface described by eq 13 approximates the shape of a teardrop (see Figure 1), with the associated Gaussian curvature

$$K = \left(\frac{p}{2\sigma}\right)^2 - \left(\frac{q}{2\pi\sigma r^2}\right)^2 \tag{14}$$

The first (isotropic) term on the right-hand side of eq 14 is constant and equal to the squared mean curvature, $H^2 = K_{max} = (p/2\sigma)^2$. The second (deviatoric) term accounts for the spatial gradient in K. The Gaussian curvature vanishes ($K = 0$) at a distance

$$r_0 = \sqrt{q/\pi p} \tag{15}$$

from the q-source and monotonically increases up to a plateau ($K = K_{max}$) as $r \to \infty$.

Substituting eq 14 into 12 determines the force on an inclusion embedded in this model interface. Infinitely rigid inclusions ($R \ll R_B$) are driven up gradients in K and are therefore *repelled* from the q-source. Inclusions that are bending-limited ($R_B \ll R \ll R_S$) are likewise repelled, albeit more weakly. Stretching-limited inclusions ($R_B \ll R_S \ll R$), on the other hand, are driven down gradients in K^2 such that they are *attracted* to the circumference of zero Gaussian curvature, $r = r_0$. Substituting the maximum Gaussian curvature, $K_{max} = H^2$, into eq 11 yields the minimum size, $R_{S,min}$, for an inclusion to be attracted to $r = r_0$ (otherwise, it would be driven toward $r \to \infty$). For a continuum, incompressible material, eqs 3 (with $\nu = \frac{1}{2}$) apply and $R_{S,min}$ is given by

$$R_{S,min} = 2\sqrt{h/H} \tag{16}$$

https://doi.org/10.1021/acs.langmuir.1c02709
Langmuir 2022, 38, 1099−1105

which is proportional to the geometric mean of h, the characteristic inclusion thickness, and H^{-1}, the characteristic radius of curvature.

A key feature of eqs 13 and 14 is the inflection line at $r = r_0$, where the Gaussian curvature changes sign. As discussed above, this feature discriminates between static, equilibrium configurations of elastic inclusions limited by either bending or stretching. For eq 13 to hold, the radius, a, along which the force, q, is applied must be much smaller than r_0: $a \ll r_0$. Were this condition not met, then the "point-like" force, q, would be replaced with the more general expression, $q - \pi a^2 p$, to account for the finite size of the central source. For source radii $a = O(r_0)$ [or, equivalently, $\pi a^2 p = O(q)$], the inflection line is eliminated and the bending- and stretching-limited regimes cannot be distinguished based solely upon the static positions of inclusions within the interface.

The strength of the curvature gradient is controlled by the pulling (or pushing) force, q. Such forces could be realized experimentally by drawing a cylindrical filament of radius a out of (or into) a small droplet; the force is then given by $q = 2\pi\sigma a \cot \alpha$, where α is the angle measured from the cylinder boundary to the fluid interface through the droplet phase. With such a strategy, the main challenge is to achieve small contact angles, α (i.e., large forces, q), while also minimizing the filament radius, a, to promote large curvature gradients. In practice, the minimum contact angle would typically be limited by the wetting properties of the filamentous material.

In the seminal experiments of Cavallaro et al.,[34] a central micropost was used to pin an initially planar water−oil interface to a cylindrical radius $a = 131\ \mu$m, achieving contact angles $\alpha \approx 70°$ and forces $q \approx 15\ \mu$N. In their system, the interface has zero mean curvature ($H = 0$), giving a radius $r_0 \to \infty$ according to eq 15. Hence, the region far from the post, where the Gaussian curvature vanishes, also coincides with the maximum possible Gaussian curvature, $K_{max} = H^2 = 0$. This represents yet another scenario where one expects both the bending- and stretching-limited responses to produce the same equilibrium positions of elastic inclusions. In such cases where static measurements yield limited information, a potential alternative is to track the motion of the inclusions along the interface as a function of time. Such *dynamic* measurements may be more elucidating, as one expects forces and velocities $\propto \nabla K$ in the bending-limited regime and $\propto -\nabla K^2$ in the stretching-limited regime.

Energy Landscapes. For systems at finite temperature, it is useful to express the force, $\boldsymbol{F} = -\nabla U$, in terms of a potential energy landscape, $U(\boldsymbol{r})$, whose strength can be compared against the thermal energy, kT. We can evaluate this energy for the model interface described by eq 13, assuming the static pressure, $p = -2\sigma H$, is finite. Integrating eq 12, with 14 substituted for $K(\boldsymbol{r})$, directly gives $U(\boldsymbol{r})$. Its limiting forms for *deformable* inclusions are likewise obtained by integrating eqs 8b and 10:

$$U = U_B\left(\frac{r_0}{r}\right)^4, \quad R \ll R_{S,min} \tag{17a}$$

$$U = U_S\left[\left(\frac{r_0}{r}\right)^8 - 2\left(\frac{r_0}{r}\right)^4\right], \quad R \gg R_{S,min} \tag{17b}$$

where r_0 is given by eq 15 and

$$U_B = \frac{1}{2}(1-\nu)BR^2H^2 \tag{18a}$$

$$U_S = \frac{1}{384}SR^6H^4 \tag{18b}$$

are the energy scales for bending and stretching, respectively. The resulting energy profiles are plotted in Figure 4 for inclusion radii smaller or larger than $R_{S,min}$ (cf. eq 16), as measured by the ratio $R/R_{S,min} = (U_S/U_B)^{1/4}$. Notably, the stretching-limited energy exhibits an attractive well of depth U_S centered at $K = 0$, as predicted by eq 17b. The depth of the well decreases as the inclusion radius is decreased and vanishes asymptotically as $R/R_{S,min} \to 0$, resulting in a purely repulsive energy landscape (eq 17a).

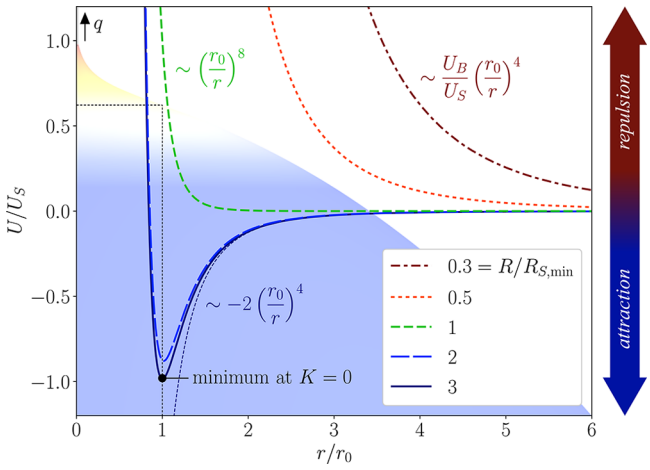

Figure 4. Potential energy landscapes, assuming $SR^2H^2/\sigma \ll 1$, for the model interface described by eq 13 (for reference, the shape of the interface is illustrated in the background; see also Figure 1). Line styles and colors indicate different values of $R/R_{S,min}=(U_S/U_B)^{1/4}$. The two limiting forms of the energy are given by eqs 17.

As a model material system, we consider a thin elastomer trapped at the oil−water interface of a solid-supported, microscopic droplet ($|H|^{-1} = 100\ \mu$m, $h = 1\ \mu$m, $E = 1$ MPa, $\nu = 0.5$, $\sigma = 50$ mN/m). For this system, one estimates $R_{S,min} \approx \frac{40}{3}R_B \approx 20\mu$m from eqs 3, 7, and 11. Inclusions of radius $R > R_{S,min}$ are deformable, limited by stretching, and attracted to regions of zero Gaussian curvature. Using eqs 18 and taking $R = R_{S,min} \approx 20\ \mu$m (exactly at the stretching crossover threshold) gives an energy scale, $U_B = U_S \sim 10^5\ kT$, that is much larger than the thermal energy. One therefore expects inclusions of this size and stiffness to follow deterministic trajectories along the curvature landscape, provided that the curvature gradients are sufficiently strong.

CONCLUSIONS

We have analyzed the forces on *deformable*, solid inclusions in curved fluid interfaces, extending prior findings for rigid particles. Our analysis of the Föppl−von Kármán equations yielded forces $\boldsymbol{F} \propto \nabla K$ (eq 8) in cases where the solid deformation is limited by resistance to bending and $\boldsymbol{F} \propto -\nabla K^2$ (eq 10) when limited by stretching. These two outcomes can be distinguished by examining either the static or dynamic behavior of elastic inclusions on interfaces of well-defined, anisotropic curvature. All of our predictions collapse onto a

https://doi.org/10.1021/acs.langmuir.1c02709
Langmuir 2022, 38, 1099−1105

semiempirical, universal curve (eq 12) that reproduces the bending- and stretching-limited asymptotics.

Our analysis also revealed that the characteristic size, R, of elastic inclusions is a key determinant of their ability to bend or stretch. We have identified two important length scales, R_B (eq 7) and R_S (eq 11), that, when compared to R, determine whether (and how) an interface-embedded inclusion deforms. Likewise, the energy scales, U_B and U_S (eqs 18), gauge the strength of the resulting curvature-mediated forces based on the maximum Gaussian curvature, $K_{max} = H^2$ (the actual strength also depends, of course, on the local *gradient* of Gaussian curvature). The relative importance of stretching compared to bending is reflected in the ratio $R/R_{S,min}$ or, equivalently, U_S/U_B. Increasing either the characteristic thickness, h ($\sim\sqrt{B/S}$), or the radius of curvature, H^{-1}, will increase $R_{S,min}$ and, for fixed R, decrease $R/R_{S,min}$.

The theory presented herein neglects any intrinsic curvature of the solid inclusions—that is, they are planar in their stress-free state. Such intrinsic curvature could be induced by the "spontaneous curvature" of the 2D solid phase (e.g., solid domains in asymmetric monolayers and bilayers) or by edge interactions with the 2D fluid phase (e.g., interface-trapped particles with contact-line undulations).[30,34,35] According to the Donnell–Mushtari–Vlasov (DMV) theory of shallow, elastic shells[47] (a natural extension of the Föppl–von Kármán theory for elastic plates), a curved shell placed in a tension field will experience stresses that resist changes to its intrinsic curvature. Without performing any detailed calculation, it seems reasonable to expect that intrinsically curved inclusions will be attracted to interfacial regions of similar Gaussian curvature (in our analysis, an initially planar inclusion will focus to regions of *zero* Gaussian curvature). Indeed, this outcome was predicted by Aharoni et al.[45] in their analysis of geometrically frustrated, elastic disks embedded in curved subspaces. Thus, the interaction between the curvature of the fluid interface and the intrinsic curvature of a dispersed, solid phase is an interesting problem that merits further investigation.

■ ASSOCIATED CONTENT

Supporting Information

The Supporting Information is available free of charge at https://pubs.acs.org/doi/10.1021/acs.langmuir.1c02709.

Governing equations and boundary conditions; numerical method and calculations for finite pressures; analysis for the bending- and stretching-limited regimes (PDF)

■ AUTHOR INFORMATION

Corresponding Author

Todd M. Squires − *Department of Chemical Engineering, University of California, Santa Barbara, California 93106, United States;* orcid.org/0000-0001-6609-9275; Email: squires@engineering.ucsb.edu

Author

Joseph M. Barakat − *Department of Chemical Engineering, University of California, Santa Barbara, California 93106, United States;* orcid.org/0000-0001-7761-3874

Complete contact information is available at: https://pubs.acs.org/10.1021/acs.langmuir.1c02709

Notes

The authors declare no competing financial interest.

■ ACKNOWLEDGMENTS

The research reported in this publication was supported by the National Heart, Lung, and Blood Institute of the National Institutes of Health (Grant No. R01HL135065). J.M.B. was supported by the NIH F32 Ruth L. Kirschstein National Research Service Award (Grant No. F32HL156366). The content is solely the responsibility of the authors and does not necessarily represent the official views of the National Institutes of Health.

■ REFERENCES

(1) McConnell, H. M.; Tamm, L. K.; Weis, R. M. Periodic structures in lipid monolayer phase transitions. *Proc. Natl. Acad. Sci. U. S. A.* **1984**, *81*, 3249−3253.

(2) Helm, C. A.; Möhwald, H.; Kjaer, K.; Als-Nielsen, J. Phospholipid monolayers between fluid and solid states. *Biophysical journal* **1987**, *52*, 381−390.

(3) Ding, J.; Warriner, H. E.; Zasadzinski, J. A. Viscosity of two-dimensional suspensions. *Phys. Rev. Lett.* **2002**, *88*, 168102.

(4) Espinosa, G.; López-Montero, I.; Monroy, F.; Langevin, D. Shear rheology of lipid monolayers and insights on membrane fluidity. *Proc. Natl. Acad. Sci. U. S. A.* **2011**, *108*, 6008−6013.

(5) Sachan, A.; Choi, S. Q.; Kim, K.; Tang, Q.; Hwang, L.; Lee, K.; Squires, T.; Zasadzinski, J. Interfacial rheology of coexisting solid and fluid monolayers. *Soft Matter* **2017**, *13*, 1481−1492.

(6) Korlach, J.; Schwille, P.; Webb, W. W.; Feigenson, G. W. Characterization of lipid bilayer phases by confocal microscopy and fluorescence correlation spectroscopy. *Proc. Natl. Acad. Sci. U. S. A.* **1999**, *96*, 8461−8466.

(7) Veatch, S. L.; Keller, S. L. Miscibility phase diagrams of giant vesicles containing sphingomyelin. *Physical review letters* **2005**, *94*, 148101.

(8) Hirst, L. S.; Uppamoochikkal, P.; Lor, C. Phase separation and critical phenomena in biomimetic ternary lipid mixtures. *Liq. Cryst.* **2011**, *38*, 1735−1747.

(9) Chen, D.; Santore, M. M. Large effect of membrane tension on the fluid−solid phase transitions of two-component phosphatidylcholine vesicles. *Proc. Natl. Acad. Sci. U. S. A.* **2014**, *111*, 179−184.

(10) Xin, W.; Wu, H.; Grason, G. M.; Santore, M. M. Switchable positioning of plate-like inclusions in lipid membranes: Elastically mediated interactions of planar colloids in 2D fluids. *Science Advances* **2021**, *7*, No. eabf1943.

(11) Bacia, K.; Scherfeld, D.; Kahya, N.; Schwille, P. Fluorescence correlation spectroscopy relates rafts in model and native membranes. *Biophysical journal* **2004**, *87*, 1034−1043.

(12) Simons, K.; Vaz, W. L. Model systems, lipid rafts, and cell membranes. *Annu. Rev. Biophys. Biomol. Struct.* **2004**, *33*, 269−295.

(13) Ursell, T. S.; Klug, W. S.; Phillips, R. Morphology and interaction between lipid domains. *Proc. Natl. Acad. Sci. U. S. A.* **2009**, *106*, 13301−13306.

(14) Regen, S. L. The Origin of Lipid Rafts. *Biochemistry* **2020**, *59*, 4617−4621.

(15) Vénien-Bryan, C.; Lenne, P.-F.; Zakri, C.; Renault, A.; Brisson, A.; Legrand, J.-F.; Berge, B. Characterization of the growth of 2D protein crystals on a lipid monolayer by ellipsometry and rigidity measurements coupled to electron microscopy. *Biophys. J.* **1998**, *74*, 2649−2657.

(16) Ratanabanangkoon, P.; Gropper, M.; Merkel, R.; Sackmann, E.; Gast, A. P. Two-dimensional streptavidin crystals on giant lipid bilayer vesicles. *Langmuir* **2002**, *18*, 4270−4276.

(17) Ford, M. G.; Mills, I. G.; Peter, B. J.; Vallis, Y.; Praefcke, G. J.; Evans, P. R.; McMahon, H. T. Curvature of clathrin-coated pits driven by epsin. *Nature* **2002**, *419*, 361−366.

(18) Stachowiak, J. C.; Schmid, E. M.; Ryan, C. J.; Ann, H. S.; Sasaki, D. Y.; Sherman, M. B.; Geissler, P. L.; Fletcher, D. A.; Hayden, C. C. Membrane bending by protein−protein crowding. *Nature cell biology* **2012**, *14*, 944−949.
(19) Irvine, W. T.; Vitelli, V.; Chaikin, P. M. Pleats in crystals on curved surfaces. *Nature* **2010**, *468*, 947−951.
(20) Meng, G.; Paulose, J.; Nelson, D. R.; Manoharan, V. N. Elastic instability of a crystal growing on a curved surface. *Science* **2014**, *343*, 634−637.
(21) Paquay, S.; Both, G.-J.; van der Schoot, P. Impact of interaction range and curvature on crystal growth of particles confined to spherical surfaces. *Phys. Rev. E* **2017**, *96*, 012611.
(22) Landau, L. D.; Lifshitz, E. M. *Theory of Elasticity; Course of Theoretical Physics*; Pergamon Press, 1959; Vol. 7.
(23) Davidovitch, B.; Sun, Y.; Grason, G. M. Geometrically incompatible confinement of solids. *Proc. Natl. Acad. Sci. U. S. A.* **2019**, *116*, 1483−1488.
(24) Schneider, S.; Gompper, G. Shapes of crystalline domains on spherical fluid vesicles. *EPL (Europhysics Letters)* **2005**, *70*, 136.
(25) Phillips, R.; Kondev, J.; Theriot, J.; Garcia, H. G.; Orme, N. *Physical Biology of the Cell*; Garland Science, 2012.
(26) Bassereau, P.; et al. The 2018 biomembrane curvature and remodeling roadmap. *J. Phys. D: Appl. Phys.* **2018**, *51*, 343001.
(27) Notter, R. H. *Lung Surfactants: Basic Science and Clinical Applications*; CRC Press, 2000.
(28) Huang, C.; Forth, J.; Wang, W.; Hong, K.; Smith, G. S.; Helms, B. A.; Russell, T. P. Bicontinuous structured liquids with sub-micrometre domains using nanoparticle surfactants. *Nature Nanotechnol.* **2017**, *12*, 1060−1063.
(29) Mohraz, A. Simple shaking yields bicontinuity. *Nature Nanotechnol.* **2017**, *12*, 1021−1022.
(30) Stamou, D.; Duschl, C.; Johannsmann, D. Long-range attraction between colloidal spheres at the air-water interface: The consequence of an irregular meniscus. *Phys. Rev. E* **2000**, *62*, 5263.
(31) Würger, A. Curvature-induced capillary interaction of spherical particles at a liquid interface. *Phys. Rev. E* **2006**, *74*, 041402.
(32) Ershov, D.; Sprakel, J.; Appel, J.; Cohen Stuart, M. A.; van der Gucht, J. Capillarity-induced ordering of spherical colloids on an interface with anisotropic curvature. *Proc. Natl. Acad. Sci. U. S. A.* **2013**, *110*, 9220−9224.
(33) Blanc, C.; Fedorenko, D.; Gross, M.; In, M.; Abkarian, M.; Gharbi, M. A.; Fournier, J.-B.; Galatola, P.; Nobili, M. Capillary force on a micrometric sphere trapped at a fluid interface exhibiting arbitrary curvature gradients. *Physical review letters* **2013**, *111*, 058302.
(34) Cavallaro, M.; Botto, L.; Lewandowski, E. P.; Wang, M.; Stebe, K. J. Curvature-driven capillary migration and assembly of rod-like particles. *Proc. Natl. Acad. Sci. U. S. A.* **2011**, *108*, 20923−20928.
(35) Sharifi-Mood, N.; Liu, I. B.; Stebe, K. J. Curvature capillary migration of microspheres. *Soft Matter* **2015**, *11*, 6768−6779.
(36) Barakat, J. M.; Squires, T. M. Capillary force on an 'inert'colloid: a physical analogy to dielectrophoresis. *Soft Matter* **2021**, *17*, 3417−3442.
(37) Bowden, N.; Terfort, A.; Carbeck, J.; Whitesides, G. M. Self-assembly of mesoscale objects into ordered two-dimensional arrays. *Science* **1997**, *276*, 233−235.
(38) Goggin, D. M.; Bei, R.; Anderson, R.; Gómez-Gualdrón, D. A.; Samaniuk, J. R. Stacking of Monolayer Graphene Particles at a Water−Vapor Interface. *J. Phys. Chem. C* **2021**, *125*, 7880−7888.
(39) Py, C.; Reverdy, P.; Doppler, L.; Bico, J.; Roman, B.; Baroud, C. N. Capillary origami: spontaneous wrapping of a droplet with an elastic sheet. *Physical review letters* **2007**, *98*, 156103.
(40) Bico, J.; Roman, B.; Moulin, L.; Boudaoud, A. Elastocapillary coalescence in wet hair. *Nature* **2004**, *432*, 690−690.
(41) Huang, J.; Juszkiewicz, M.; De Jeu, W. H.; Cerda, E.; Emrick, T.; Menon, N.; Russell, T. P. Capillary wrinkling of floating thin polymer films. *Science* **2007**, *317*, 650−653.
(42) Mansfield, E. H. *The Bending and Stretching of Plates*; Cambridge University Press, 1989.
(43) Domínguez, A.; Oettel, M.; Dietrich, S. Force balance of particles trapped at fluid interfaces. *J. Chem. Phys.* **2008**, *128*, 114904.
(44) Style, R. W.; Jagota, A.; Hui, C.-Y.; Dufresne, E. R. Elastocapillarity: Surface tension and the mechanics of soft solids. *Annual Review of Condensed Matter Physics* **2017**, *8*, 99−118.
(45) Aharoni, H.; Kolinski, J. M.; Moshe, M.; Meirzada, I.; Sharon, E. Internal stresses lead to net forces and torques on extended elastic bodies. *Physical review letters* **2016**, *117*, 124101.
(46) King, H.; Schroll, R. D.; Davidovitch, B.; Menon, N. Elastic sheet on a liquid drop reveals wrinkling and crumpling as distinct symmetry-breaking instabilities. *Proc. Natl. Acad. Sci. U. S. A.* **2012**, *109*, 9716−9720.
(47) Sanders, J. L., Jr. Nonlinear theories for thin shells. *Quarterly of Applied Mathematics* **1963**, *21*, 21−36.

https://doi.org/10.1021/acs.langmuir.1c02709
Langmuir 2022, 38, 1099−1105